ChemPubSoc Europe

DOI: 10.1002/celc.201900564

CHEMELECTROCHEM Articles

Transforming Single-Crystal CuO/Cu_2O Nanorods into Nano-Polycrystalline Cu/Cu_2O through Lithiation

Pu Hu,[a] Maxim Dorogov,[b] Yan Xin,[c] and Katerina E. Aifantis*[a]

One-dimensional single-crystal CuO/Cu_2O nanorods were fabricated by controlled oxidation of a copper substrate and examined as the active material in porous anodes for lithium-ion batteries. Electrochemical testing against Li-metal revealed that using sodium carboxyl methyl cellulose (CMC) as the binder enabled an excellent capacity retention for 50 cycles, while the use of polyvinylidene fluoride (PVDF) resulted in a continuous capacity fade. Transmission electron microscopy illustrated the phase composition and morphological changes throughout cycling, revealing that for both types of binders, lithiation of CuO and Cu_2O disrupted the single-crystal nanorod structure, producing multiple Cu/Cu_2O nanograins within the rods. With continuous cycling the average grain size of these nanocrystals decreased. A significant difference between the CMC and PVDF binder electrodes was the irreversible formation of LiCuO during delithiation for the PVDF case, which can explain the continuous capacity fade. Scanning electron microscopy also revealed microcracks throughout the electrode surface when the PVDF binder was employed.

1. Introduction

Transition metal oxides (TMOs) (TM = Co, Fe, Ni, Cu etc.) have attracted considerable interest as anode materials for Li-ion batteries since the early 2000s when a reversible "conversion reaction" between TMOs and Li was proposed.[1] Among TMOs, copper oxides (CuO and Cu_2O) are promising candidates due to their high theoretical capacity (which can reach 673 mAh/g for CuO and 374 mAh/g for Cu_2O), modest cost, safety and non-toxicity.[2] Upon lithiation of CuO or Cu_2O the Li^+ bonds with the O^{2-} to form Li_2O and the Cu disperses as nanoparticles within it, while upon de-lithiation the Li–O bond in Li_2O breaks and the O rebonds with Cu to form Cu_xO nanoparticles. During the lithiation process the volume changes that the CuO anode undergoes are ~174%;[3] while for Cu_2O they have not been measured. Although these volume changes are not as high as for Si and Sn anodes, for which they are over 300%, they can still cause fracture, and hence loss of electronic connectivity within the electrode, which leads to fast capacity decay upon cycling. For example, 90 nm Cu_2O film anodes had an initial capacity of 250 $mAhg^{-1}$ which decreased to 60 $mAhg^{-1}$ after 50 cycles at a current rate of 0.1 C. SEM images illustrated crack formation on the surface of the Cu_2O film electrode after cycling.[4]

In order to improve the mechanical stability, kinetics of the electrochemical reactions and charge transfer in the electrode material, battery developers have began designing one dimensional/1D (high-aspect ratio) active materials.[5] For example, CuO arrays supported on a Cu substrate (fabricated from $Cu_2(OH)_3NO_3$ precursors by thermal annealing) demonstrated a high capacity of 650 $mAh\,g^{-1}$ at 0.5 C and almost 100% capacity retention over 100 cycles.[6] While nanotube arrays of 1D Cu_2O deposited electrochemically on a Ni substrate retained a stable capacity of ~375 $mAh\,g^{-1}$ after 30 cycles.[7] A full battery using a CuO array as a binder-free anode and 5-V spinel $LiNi_{0.5}Mn_{1.5}O_4$ as the cathode delivered a reversible capacity of 660 $mAhg^{-1}$ and energy density of 217 Wh kg^{-1} at room temperature, while the average loading density of the CuO active materials was 0.8 mg cm^{-2}.[8] The drawback in commercializing the CuO arrays of [7,8] is that they exhibit good capacity when they are used directly as an integrated electrode, however, for porous electrodes the binder and additives must be included which increase the mass loading and hence reduce the capacity. For porous electrodes, the electrochemical performance not only depends on the intrinsic properties of the active materials, such as the morphology and particle size, but also on the binder, conductive additives and current collector. The mechanical properties of the binder have a significant impact on the electrochemical stability of the electrode materials, especially for electrodes that experience large volume changes during charge/discharge.[9] It has been recently shown that using sodium carboxyl methyl cellulose (CMC) as the binder in CuO electrodes allows for a better cycling stability than when using polyvinylidene fluoride (PVDF). For example, 2–3 μm CuO particles with a PVDF binder exhibited a rapid capacity decay from 625 $mAh\,g^{-1}$ to 199 $mAh\,g^{-1}$ after 100 cycles (32% capacity retention), while employing CMC as the binder, allowed the capacity retention to be 92% after the same cycles.[10] In order to understand the underlying mechanisms that allow CMC to give an increased capacity stability, 1D

[a] Dr. P. Hu, Dr. K. E. Aifantis
Department of Mechanical and Aerospace Engineering, University of Florida, Gainesville, 32603, USA
E-mail: kaifantis@ufl.edu
[b] Dr. M. Dorogov
Togliatti State University, Togliatti, Russian Federation, Togliatti, 445667, Russia
[c] Dr. Y. Xin
National High Magnetic Field Laboratory, Florida State University, Tallahassee, 32310, USA

Supporting information for this article is available on the WWW under https://doi.org/10.1002/celc.201900564

structured CuO/Cu_2O nanorods were applied herein as the active materials in porous electrodes considering either CMC or PVDF as the binder. Transmission electron microscopy (TEM) and selected area electron diffraction (SAED) were used to capture the composition of the electrodes at various cycles and reveal how the lithiation process of CuO/Cu_2O nanorods depends on the binder.

2. Results and Discussion

The X-ray diffraction (XRD) spectrum in Figure 1a, illustrates that prior cycling all diffraction peaks could be indexed into

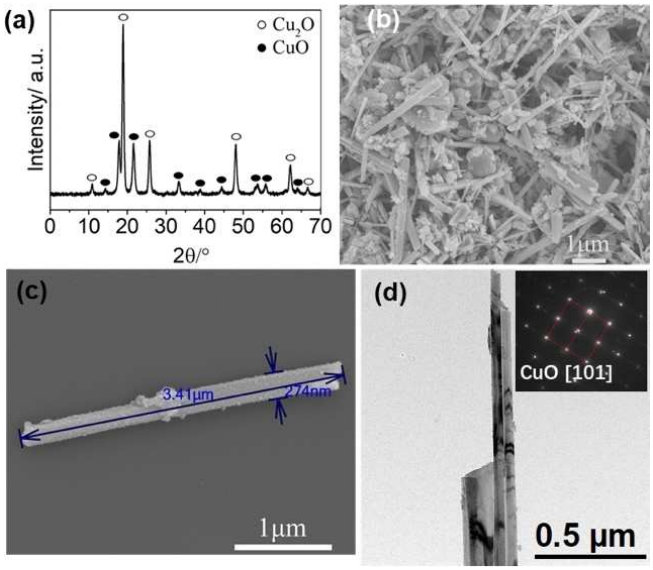

Figure 1. (a) XRD spectrum of as prepared CuO/Cu_2O nanorods. (b) and (c) SEM images of as prepared nanorods without Cu substrate. (d) TEM bright field image of nanorods, inset of (d) shows SAED pattern of another rod of CuO [101].

cubic Cu_2O (JCPDF card no. 05–0667) and monoclinic CuO (JCPDF card no. 48–1548), which indicates that Cu metal was successfully oxidized to copper oxide during heat treatment. The diffraction peaks located at 29.5°, 36.4°, 42.3°, 61.3° and 73.5° are associated with the (110), (111), (200), (220) and (311) reflections of cuprite Cu_2O, which is the main phase of the powders. No impurity peaks were found, implying that the Cu substrate had been completely removed by ultrasonic treatment.

The scanning electron microscopy (SEM) images of Figure 1b and c present the nanorods after they were removed from the substrate. The length and diameter of the nanorods remained intact, indicating that the ultrasonic approach didn't destroy their 1D nanostructure. The typical nanorods shown in Figure 1c and d had a diameter of approximately 274 nm and length up to 3.4 μm, demonstrating a high aspect ratio of the 1D nanostructures. To further confirm the crystal structure, selected area electron diffraction (SAED) (Figure 1d) was performed, which demonstrated that the rods were single crystal. The diffraction spots were measured to have a d-spacing of 2.34 and 2.37 Å and an angle of 85°, and they could be indexed to be the (−111) and (11-1) planes of [101] CuO, demonstrating that this particular nanorod was CuO. It was not possible to detect the Cu_2O phase in the TEM for the few individual nanorods examined, which is probably due to the limitation of microcosmic observation area by TEM sampling.

To verify that fabrication of the porous electrode did not alter the microstructure of the nanorods shown in Figure 1, TEM images of the porous electrodes prior cycling are shown in Figure 2a. It is seen that the Cu_2O/CuO nanorod retained its flat

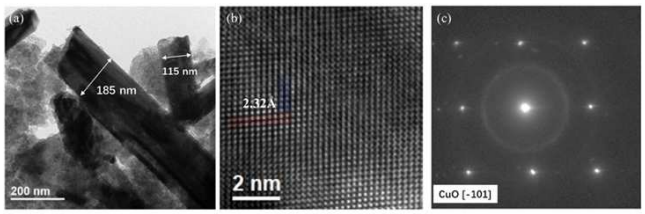

Figure 2. (a) TEM image, (b) HR-TEM images and (c) SAED pattern along [101] for one CuO nanorod before electrochemical cycling.

surface with good structural integrity and a diameter of ~100–200 nm. Amorphous carbon was present in-between the nanorods to build an interconnected conductive network. High-resolution TEM (HR-TEM) imaging (Figure 2b) and its corresponding SAED pattern (Figure 2c) revealed that the nanorods retained their perfect single-crystal structure. The well-defined lattice fringes with a lattice space of 2.32 Å, close to (−111) planes of monoclinic CuO, indicated that the nanorod was grown along the $<111>$ direction.

The electrochemical performance of the porous electrodes is shown in Figure 3a–c. Here, we independently compared the

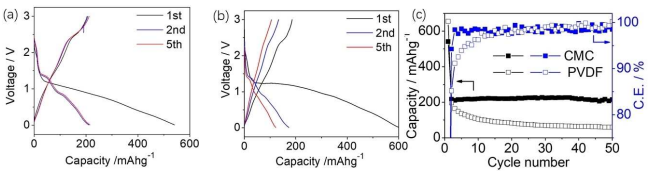

Figure 3. Discharge/charge curves of Cu_2O/CuO nanorods combined with (a) CMC binder and (b) PVDF binder, between 0.01–3.0 V at current density of 33.7 mAg^{-1}; (c) cycling performance of Cu_2O/CuO nanorods.

electrochemical stability and electrode integrity of Cu_2O/CuO porous electrode using CMC (Figure 3a) or PVDF (Figure 3b) as the binder. A long plateau is observed during the first discharge cycle for both cases, implying that a reduction reaction took place between Cu_2O/CuO and Li, which could be described as:

$$Cu_2O + 2Li \rightarrow 2Cu + Li_2O \quad (1)$$

$$CuO + 2Li \rightarrow Cu + Li_2O \quad (2)$$

The first discharge and charge capacities of the Cu_2O/CuO electrode using CMC as the binder (Figure 3a) are 541 mAh g^{-1} and 204 mAh g^{-1}, respectively, corresponding to an initial Coulombic efficiency of 37.7%. The large irreversible capacity loss in the first electrochemical cycle could be attributed to the decomposition of the organic electrolyte and formation of solid-electrolyte interface (SEI) layer and partially irreversible formation of Li_2O. With continuous cycling, the charge-discharge curves of each cycle remained similar in shape and a high Coulombic efficiency of ~99% was observed, indicating a reversible electrochemical process.

For comparison, charge-discharge curves of the porous Cu_2O/CuO electrode using PVDF as the binder is presented in Figure 3b. The initial reversible capacity and the Coulombic efficiency were 197 mAh g^{-1} and 30.1% respectively, which is lower than when CMC was the binder. Figure S1 shows the cyclic voltammetry (CV) curves for the first two cycles of the electrode, using either CMC or PVDF as the binder, at a scan rate of 0.2 mV/s. Two cathodic peaks located at 1.15 V and 0.80 V could be attributed to a multistep electrochemical reaction, corresponding to the formation of Cu_2O phase for the first step and a reduction of Cu_2O into Cu for the second step. For the CMC-based electrode, the voltage response of the second scan coincides well with the first scan, while for the PVDF case the voltage response for the first scan is much lower than that of the second, implying a high irreversible capacity loss. Figure 3c compares the capacity retention of CMC and PVDF based Cu_2O/CuO electrodes. It is evident that the CMC binder resulted in a superior capacity retention with a stable capacity of about 217 mAh g^{-1} from the second cycle onwards. In contrast, the electrode using PVDF as the binder exhibited a fast capacity decay with each cycle. The capacity decreased from 197 mAh g^{-1} at the second cycle to 60 mAh g^{-1} after 50 cycles. The CMC-based electrode displayed a higher coulombic efficiency than the PVDF-based electrode during the initial 15 cycles. It can be particularly seen that the CMC-based electrode delivered a 99% Coulombic efficiency aside from the first cycle, while for the PVDF-based electrode the Coulombic efficiency gradually increased from 90% to 99% from the 2nd to 15th cycle and then remained at a stable value. Both the CMC and PVDF based electrodes show a similar capacity retention with an increasing current density (Figure S2).

To explore why the two binders resulted in a significantly different electrochemical performance, SEM was performed on cells cycled 1, 3 and 50 times for both PVDF and CMC binders. It is illustrated in Figure 4 (a-d) that the PVDF-based electrode underwent loss of structural integrity during Li insertion/de-insertion, as cracks were observed from the first cycle, which grew continuously, reaching a crack gap of 27 μm, after 50 cycles, as seen in Figure 4d. Such fracture disrupted the electronic connectivity of the electrode, and therefore less material could respond to the applied voltages and participate in the lithiation reaction, leading to a continuous capacity fade. Cracks on the electrode surface also induce fracture of the SEI layer, allowing more surface to be exposed to electrolyte attack, and hence forming additional SEI, which further increases the irreversible capacity loss. On the contrary, it is seen in Figure 4e-h that using CMC binder allowed to retain the integrity of the electrode throughout cycling and did not form any noticeable cracks after 50 cycles, suggesting that the CMC binder adheres better to the Cu_2O/CuO surface, thus effectively accommodating the Cu_2O/CuO volume expansion during charge/discharge.

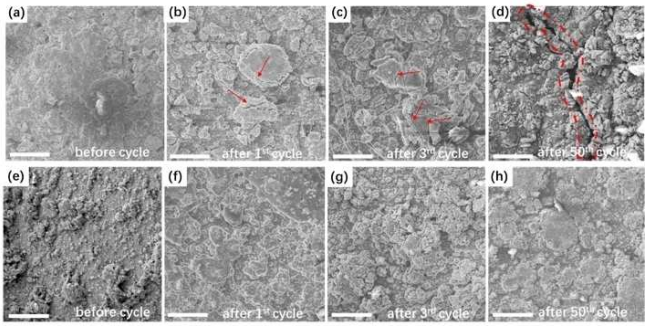

Figure 4. SEM images of electrode using (a-d) PVDF and (e-h) CMC as the binder. From left to right: before cycling and after the 1st, 3rd and 50th cycle. Scale bar: 100 μm. Red arrows indicate cracks in the PVDF case.

To further examine the microstructural evolution with cycling, TEM and HR-TEM were performed after the 1st, 3rd, and 50th cycle for both electrodes, as seen in Figures 5 and 6. All these images were taken after complete de-lithiation. Both Figures 5 and 6 reveal that after Li-insertion, the single crystal nanorods were converted to polycrystalline nanorods. This is evidenced not only from the images (comparing Figures 5&6 (a1–c1) with 5&6 (a3–c3)), but also from the SAED patterns (Figures 5&6 (a2–c2)) which showed several concentric diffraction rings, that are inherent to polycrystalline materials. Various areas of the electrode were imaged and Image J analysis was used to measure the size of the nanoparticles and produce the histograms of Figures 5&6 (a4–c4). It is seen that the particle size continuously decreased with continuous cycling.

Based on the measured d-spacing of the diffraction rings, for the CMC-based electrode, all the diffraction rings could be indexed with Cu_2O and Cu after 1, 3 and 50 cycles (Figure 5(a2), Figure 5(b2), and Figure 5(c2)), indicating that the nanoparticles comprised of Cu_2O and Cu. CuO was not detected, despite it being present prior cycling as single crystal CuO nanorods were observed both in the TEM images (Figure 1(e-f)) and XRD (Figure 1(a)). This indicates that during de-lithiation the Cu nanograins were oxidized partially to Cu_2O instead of CuO, which suggests that less O^{2-} was available for the reversible reaction to occur during de-lithiation; this is further supported by the formation of pure Cu after de-lithiation. Hence, part of the Li_2O that formed during lithiation, might be irreversible, but it was not detected as it is amorphous.

When PVDF was used as the binder, the diffraction rings (Figure 6 (a2)) were again indexed with Cu_2O and Cu after the first cycle, agreeing with the observation for the CMC case. However, unlike for the CMC base anode, tetragonal LiCuO was detected in subsequent cycling, as seen in Figure 6 (b2–c2).

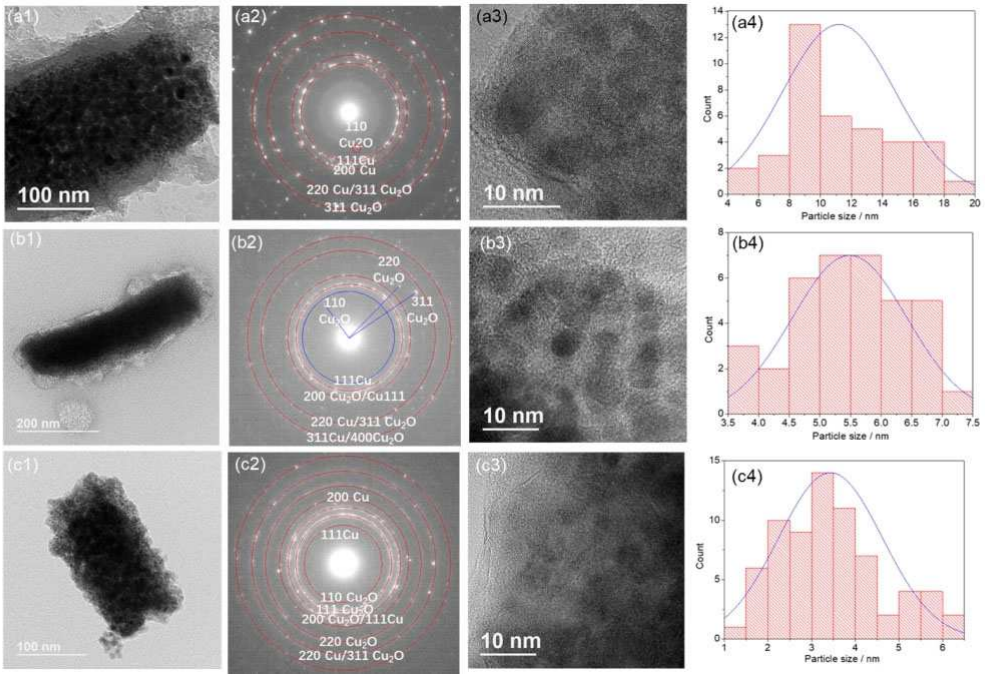

Figure 5. From left to right: Bright field (BF) TEM images of rod, the ring diffraction patterns from the rod, HR-TEM images and the particle distribution of the electrode with CMC binder after (a) 1st cycle, (b) 3rd cycle and (c) 50th cycle.

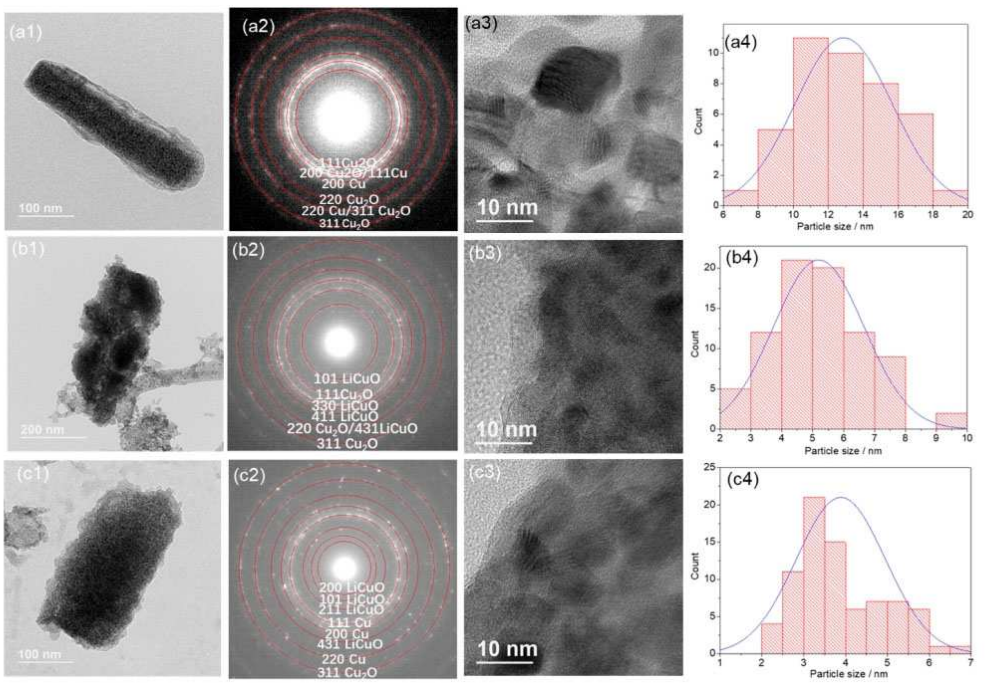

Figure 6. From left to right: BF TEM images of the rod, the ring diffraction patterns from the rod, HR-TEM images and the particle distribution of electrode with PVDF binder after the (a) 1st cycle, (b) 3rd cycle and (c) 50th cycle.

Furthermore, as shown in Figure 6(c2), the diffraction rings were mainly attributed to metallic Cu and LiCuO after 50 cycles. The increased diffraction rings for LiCuO throughout cycling correspond to an increase of LiCuO content in the anode. The increase of LiCuO content in the electrode with cycling results into the observed capacity decay, as Li remained in the anode which did not fully de-lithiate.

A histogram distribution is provided for the particle size after each cycle and the average particle size was obtained by fitting a normal distribution function, as shown in Figure 5 (a4-

c4) and Figure 6 (a4–c4). For the CMC case, the average size of the active copper oxide crystallites decreased from 11 nm to 5.5 nm and finally to 3.5 nm after the 1st, 3rd, and 50th cycle, respectively. For the PVDF case, the average active material particle size showed a similar decrease of 13 nm, 5.5 nm and 4.0 nm after the 1st, 3rd, and 50th cycle. This is a unique observation showing that with continuous cycling the grain size is refined down to a few nanometers. Although the copper oxide nanorods did not experience fracture for either binder, the structural integrity of the porous electrode was maintained only when CMC was used, as no cracks were formed on the electrode surface for that case as the SEM images in Figure 4(e–h) revealed. Nyquist plots for the electrochemical impedance spectroscopy (EIS) with different cycles are shown in Figure S3. The high-frequency depressed semicircle presents the total resistances of contact and charge transfer. The cycled electrode showed a gradual reduction of total resistance compared to the fresh (as prepared) electrode, demonstrating the activation of the electrode during charge/discharge. Although the formation of SEI layer during the first cycle could increase the resistance of the electrode during lithiation/delithiation, the transformation of nanorods into nano-polycrystalline through lithiation greatly reduces the particle size of CuO, decreasing the distance of the Li^+ diffusion path, thus reducing the impedance. For the CMC-based electrode the resistance is stable after 10 cycles.

Based on the results above, the phase transitions that the Cu_2O/CuO undergoes depend on the binder. As shown in Figure 7, the single crystal Cu_2O or CuO nanorods in the porous

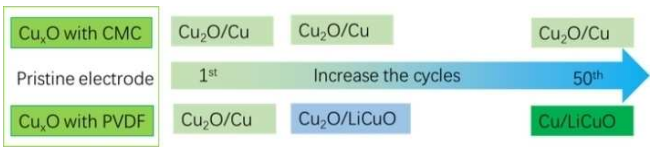

Figure 7. Illustration of the composition evolution of electrode upon cycles with different binder.

electrode with CMC binder transition into Cu_2O/Cu nanocomposites after the first the lithiation, and this structure was retained throughout cycling, allowing for a stable composition of the electrode. When PVDF binder was employed the Cu_2O/CuO nanorods underwent the same transformation into Cu_2O/Cu nanocomposites after the first cycle, however, further cycling resulted in the accumulation of LiCuO phase.

The insertion of Li^+ into CuO is accompanied by the formation of multiphase intermediates such as $Cu_{1-x}Cu_xO_{1-x/2}$, Cu_2O. At the full lithiated state, Cu nanograins were found to be uniformly dispersed into a Li_2O matrix for both CuO/Li and Cu_2O/Li cells[11]. During de-lithiation oxygen was released to partially or fully oxidized metal particles. For a typical conversion mechanism, the electrode must be composed of Cu/Li_2O upon the full lithiation. The present observations are consistent with these results, however, the de-lithiation process was not explored in [11].

During the de-lithiation process, LiCuO can be considered as an intermediate phase from Li_2O/Cu to Cu_2O. The reversible lithiation/delithiation process of the present anodes can be described by two steps as:

$$Li_2O + Cu \leftrightarrow LiCuO + Li \quad \text{(Step 1)}$$

$$LiCuO + Cu \leftrightarrow Cu_2O + Li \quad \text{(Step 2)}$$

The large irreversible capacity loss that occurred during the first cycle for both CMC and PVDF anodes can be attributed to a partly irreversible formation for Li_2O; i.e. not all the Li_2O from step 1 could take part in the reaction. The continuous capacity decay for the PVDF case is due to the accumulation of LiCuO, which results in loss of Li in the anode during each cycle. Both electrodes formed the LiCuO intermediate phase according to step 1, however, the ability to transform LiCuO into Cu_2O and Li (step 2) was shown to depend on the binder in these experiments. Based on the SAED patterns, the reversibility of step 2 for the PVDF based electrode diminished with each cycle, leading to a continuous loss of Li and corresponding capacity loss. Such a drawback did not occur when CMC was the binder, and therefore a perfect capacity retention was observed after the first cycle.

3. Conclusions

Uniform 1D Cu_2O/CuO nanorods (diameter of 100–200 nm and length of ~2 μm) were synthesized by controlled oxidation of a metal copper substrate. It is well known that these materials undergo a conversion mechanisms during lithiation, however, the effect of the binder in this process has not been explored. Herein porous electrodes with Cu_2O/CuO nanorods as the active material and either CMC or PVDF as the binder were cycled and examined with TEM and SEM after the 1st, 3rd and 50th electrochemical cycles. The CMC-based electrodes exhibited an excellent capacity retention, while the PVDF binder resulted in a continuous capacity fade. This is due to both the superior mechanical stability that CMC provided and to the fact that PVDF resulted in the formation of irreversible LiCuO. Another interesting observation is that, regardless of the binder, lithiation transformed the single crystal CuO and Cu_2O nanorods into polycrystalline nanorods whose grain size continuously decreased with cycling down to a few nm.

Experimental Section

Synthesis of CuO/Cu_2O Nanorods

The surface of a stainless steel mesh was coated with Cu through electrodeposition in an electrolyte solution consisting of 250 g/L $CuSO_4{\cdot}4H_2O$ and 90 g/L H_2SO_4. The electrodeposition was performed at an overvoltage of −160 mV for 15 min in a standard three-electrode cell, in which copper wire M0b (EN analogue Cu-OF, ASTN C10200) was used as a reference electrode, while stainless steel mesh, which was degreased with alcohol and purified by

ultrasound in distilled water, was used as the working and counter electrode, respectively. The Cu coated substrate was thoroughly rinsed with distilled water and dried in a warm air stream (60–70 °C).

Nanorods (or nanowhiskers) of copper oxide were grown on the surface of metal copper substrate by a thermal oxidation process, which was carried out in a muffle furnace at 400 °C for 4 hours in a stream of air. Finally, an ultrasonic bath was used to detach the copper oxide nanorods and create "free-standing" CuO/Cu_2O nanostructured powders. The length and diameter of the nanorods can be controlled during synthesis by adjusting the reaction time and temperature. The growth mechanism of CuO/Cu2O nanorods on Cu substrate have been published in [12].

Electrochemical Measurements

Porous electrodes were fabricated using a mixture of active material (CuO/Cu_2O), carbon black and binder in the weight ratio of 8:1:1. The CuO/Cu_2O nanorod composite, acetylene black and CMC (or PVDF) was mixed with N-methylpyrrolidone (NMP) solvent to obtain a homogeneous slurry, which was then cast onto copper current collectors, and dried at 120 °C under vacuum for 10 h. Lithium metal with 1 mm thickness was used as the counter electrode, and the solution of 1 M $LiPF_6$ in ethylene carbonate/ diethyl carbonate with volume ratio of 1:1 was used as the electrolyte. CR2032 coin-cells were assembled in an argon-filled glovebox. The cells were cycled under the constant current charging/discharging mode in the potential range of 0.01–3.0 V (vs. Li/Li^+) at a constant current density of 33.7 mAg^{-1} using an Arbin 2000 battery tester. Electrochemical impedance spectroscopy (EIS) was tested in the frequency range of 100 kHz to 100 mHz with an excitation amplitude of 5 mV.

Materials Characterization

The crystal structure of pristine nanorods was analyzed by X-ray diffraction on Shimadzu XRD 7000 diffractometer using CuKα radiation (30 kV, 30 mA, $\lambda = 1.5412$ Å) and a secondary monochromator. The morphology before and after cycling was examined using scanning electron microscopy (TESCAN, VEGA3) and transmission electron microscopy (JEM-ARM200cF). For the post cycling case, once the cells were opened, the electrode was washed with ethylene carbonate/ diethyl carbonate and dimethyl carbonate to remove the electrolyte, and then powder was scraped onto the TEM grid for TEM imaging, while the whole electrode was placed in the SEM for SEM imaging. In order to avoid the influence of Cu from conventional TEM grids, Au-mesh with carbon film grids were employed for all experiments.

Acknowledgements

Support is acknowledged from the EU-RISE program, grant No. 734485 "Fracture Across Scales and Materials, Processes and Disciplines/FRAMED". This work was initiated through the support of the Ministry of Education and Science of Russian Federation under Mega Grant No. 14.Z50.31.0039 to Togliatti State University. TEM work was performed at the National High Magnetic Field Laboratory, which is supported by National Science Foundation Cooperative Agreement No. DMR-1644779 and the State of Florida.

Conflict of Interest

The authors declare no conflict of interest.

Keywords: copper oxide · nanorods · binder · anode materials · Li-ion batteries

[1] P. Poizot, S. Laruelle, S. Grugeon, L. Dupont, J. M. Tarascon, *Nature* **2000**, *407*, 496–499.
[2] a) X. Zou, H. Fan, Y. Tian, M. Zhang, X. Yan, *Dalton Trans.* **2015**, *44*, 7811–7821; b) C. Zhong, J.-Z. Wang, X.-W. Gao, S.-L. Chou, K. Konstantinov, H.-K. Liu, *J. Nanosci. Nanotechnol.* **2012**, *12*, 1314–1317.
[3] R. Dang, X. Jia, X. Liu, H. Ma, H. Gao, G. Wang, *Nano Energy* **2017**, *33*, 427–435.
[4] A. Lamberti, M. Destro, S. Bianco, M. Quaglio, A. Chiodoni, C. F. Pirri, C. Gerbaldi, *Electrochim. Acta* **2012**, *86*, 323–329.
[5] R. Sahay, P. Suresh Kumar, V. Aravindan, J. Sundaramurthy, W. Chui Ling, S. G. Mhaisalkar, S. Ramakrishna, S. Madhavi, *J. Phys. Chem. C* **2012**, *116*, 18087–18092.
[6] Z. Wang, F. Su, S. Madhavi, X. W. Lou, *Nanoscale* **2011**, *3*, 1618–1623.
[7] M. Hasan, T. Chowdhury, J. F. Rohan, *J. Electrochem. Soc.* **2010**, *157*, A682.
[8] W. Zhang, G. Ma, H. Gu, Z. Yang, H. Cheng, *J. Power Sources* **2015**, *273*, 561–565.
[9] a) J. P. Yen, C. M. Lee, T. L. Wu, H. C. Wu, C. Y. Su, N. L. Wu, J. L. Hong, *ECS Electrochem. Lett.* **2012**, *1*, A80–A82; b) W. R. Liu, M. H. Yang, H. C. Wu, S. M. Chiao, N. L. Wu, *Electrochem. Solid-State Lett.* **2005**, *8*, A100–A103.
[10] X. Zhang, Y. Hu, D. Zhu, A. Xie, Y. Shen, *Ceram. Int.* **2016**, *42*, 1833–1839.
[11] S. Grugeon, S. Laruelle, R. Herrera-Urbina, L. Dupont, P. Poizot, J. M. Tarascon, *J. Electrochem. Soc.* **2001**, *148*, A285–A292.
[12] M. Dorogov, A. Kalmykov, L. Sorokin, A. Kozlov, A. Myasoedov, D. Kirilenko, N. Chirkunova, A. Priezzheva, A. Romanov & E. C. Aifantis, *Mater. Sci. Tech.* **2018**, *34*, 2126–2135; E. C. Aifantis, *Mater. Sci. Tech.* **2018**, *34*, 2126–2135.

Manuscript received: April 4, 2019
Revised manuscript received: May 20, 2019